

Article

Investigation of the Frozen Bath Layer under Cold Anodes

Donald Picard ^{1,*}, Jayson Tessier ², Guillaume Gauvin ³, Donald Ziegler ⁴, Houshang Alamdari ³ and Mario Fafard ¹

¹ Aluminum Research Centre—REGAL, Département de Génie Civil et de Génie des Eaux, Université Laval, Québec, QC G1V 0A6, Canada; Mario.Fafard@gci.ulaval.ca

² Aluminum Center of Excellence, Aluminerie de Deschambault, Alcoa Corporation, 1 Boul des Sources, Deschambault-Grondines, QC G0A 1S0, Canada; Jayson.Tessier@alcoa.com

³ Aluminum Research Centre—REGAL, Département de Génie des Mines, de la Métallurgie et des Matériaux, Université Laval, Québec, QC G1V 0A6, Canada; Guillaume.Gauvin@gci.ulaval.ca (G.G.); Houshang.Alamdari@gmn.ulaval.ca (H.A.)

⁴ Aluminum Center of Excellence, Alcoa Technical Center, Alcoa Corporation, 859 White Cloud Road, New Kensington, PA 15068, USA; Donald.Ziegler@alcoa.com

* Correspondence: Donald.Picard@gci.ulaval.ca; Tel.: +1-418-656-2131 (ext. 12238)

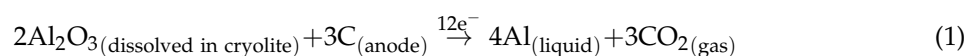
Received: 6 July 2017; Accepted: 4 September 2017; Published: 15 September 2017

Abstract: Hall-Héroult cell stability is highly affected by anode changing operations. Upon the insertion of a cold anode in the cell, a layer of molten cryolite freezes under the anode. The thickness, microstructure, and chemical composition of this layer vary as a function of time and its location in the cell. To better understand the evolution of the frozen layer, mandatory for the validation of numerical models, a measurement campaign was conducted on the anodes having a few hours of operation in the cell. The macrostructure of the selected frozen bath samples has been investigated using computed tomography while scanning electron microscope (SEM) has been used to qualify its microstructure. An energy-dispersive X-ray spectroscope (EDS) coupled to the SEM has revealed the chemical content. The results showed not only very different macrostructures between samples, but also significantly heterogeneous structure within the same sample. Nevertheless, for all samples, there is a clear distinction between the frozen cryolite and alumina/dusting phases, with the latter surrounding the cryolite matrix.

Keywords: cryolite; anode; computed tomography; microstructure; anode changing

1. Introduction

Large-scale aluminium production is based on the Hall-Héroult electrolysis process, in which alumina is dissolved in molten cryolitic bath ($\text{Na}_3\text{AlF}_6 + (\text{AlF}_3)_{\text{excess}} + \text{CaF}_2 + \text{Al}_2\text{O}_3$) [1]. The electrolysis of dissolved alumina (Al_2O_3), performed using an electrolysis cell (4–5 V and typically 200–400 kA) [2], occurs at approximately 960 °C and leads to anode carbon consumption through the global reaction defined in Equation (1). Hence, this electrode needs to be replaced after 25–27 days of operation through an anode changing operation. The lifespan of the anode may vary by a few days depending on a number of factors including cell technology.



Insertion of a new and cold anode (~25–40 °C) in a molten cryolite bath at 960 °C will disturb the stability of the cell in many ways [3–5]. From a thermal point of view, upon the insertion of the cold anode, a few centimeters of cryolitic bath will freeze under it and will melt within the next few

hours of operation. Hence, thermal balance will be affected during this period. In addition, density variation, due to cryolite phase change (solidification/fusion), will lead to bath volume changes [6,7]. Some researchers are now using numerical tools to simulate the anode change operation to estimate its impact on heat transfer in the electrolysis cell [3–5,8].

The simulation of bath phase change underneath and around the anode requires characterization of both liquid and solid bath to be able to validate those models. Recently, Poncsák et al. [9] have studied the impact of the heat flux on the solidification of unstirred cryolitic bath. They have highlighted the fact that high solidification rate can block diffusion of ions [1,6,7] and preserve the chemical composition of the bath. On the other hand, a slower solidification rate will allow more bath segregation and consequently more variation in its properties. Poncsák et al. [9] also studied two different scenarios of cryolitic bath solidification without electrolysis in a laboratory-scale experiment: A transient one where the temperature evolution of the cold anode surface (represented by a steel cold finger probe) is dictated by the bath temperature and a near steady-state one where the finger steel probe surface is stabilized at around 775 °C. The former may be more representative of the industrial case considering the large thermal inertia of carbon anodes leading to very high thermal fluxes [10]. The two case studies led to two very different frozen cryolite structures. The transient case led to two morphologically distinct solidified bath layers. The first layer, in direct contact with the probe and thus with a high cooling rate, is dense with a relatively homogeneous morphology. The cooling rate of the second layer was lower and led instead to a brittle porous structure. In the near steady-state case, similar observations have been made but with less morphological variations between the high and low cooling rate zones. The structure and composition of the frozen cryolitic bath are hence highly correlated with the heat transfer occurring near cold surfaces [9,11,12].

As pointed out previously, chemical composition and morphology of frozen cryolitic bath are highly heat flux dependent. Both can affect the frozen cryolite density thus the volume change estimation, which is a very useful parameter in numerical model calibration [8]. However, based on plant observations, at least another phenomenon must be taken into account in the frozen bath apparent density evaluation: Gas trapped in the frozen cryolite. Thus, the objective of this work is to analyze the morphology of a frozen bath sample, taken from industrial anode after few hours of operation, to get insights of the influence of operational conditions on chemical composition and apparent density of the frozen bath. The origin of the trapped gas is still under investigation and will not be discussed here, but a likely supersaturation in CO₂ near the electrode would result in different results from experiments with and without electrolysis.

2. Materials and Methods

Solidified bath samples were taken from anodes after only a few hours of operation at Alcoa Deschambault smelter (Alcoa Corporation, Québec, QC, Canada). Frozen bath morphology highly depends on the anode's history, i.e., anode initial temperature, position in the cell, surface integrity, cell stability, alumina concentration and distribution, etc. All those parameters can affect the heat flux and bath composition near the newly inserted anodes. In addition, dusting events in the cell can also influence samples' morphology. Knowing all these, two very different samples from different anodes and operating time of those anodes have been chosen and are presented in Figure 1. Those two samples, coming from two different reactors, are representative of most of the morphologies found in a batch of 50 frozen bath samples and were removed from anodes located near the center of their corresponding cell after approximately 5 h of operating time. Sample A was chosen based on the fact that its structure seems to be relatively homogeneous with a minimum of porosity (from outside observation). On the other hand, sample B was selected based on its very porous structure and its near constant thickness. In both cases, the sample surface in contact with the anode was slightly damaged while removing the sample but the overall integrity has been kept as well as sample orientation.

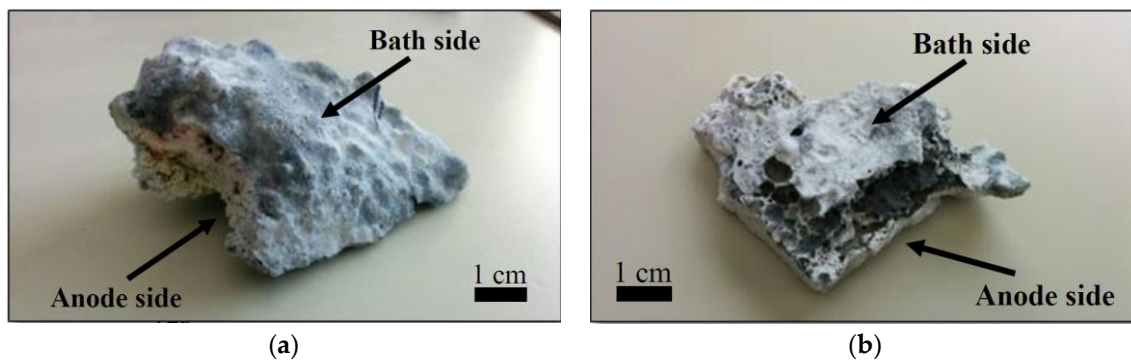


Figure 1. Photos of the frozen bath: (a) Sample A and (b) sample B. The bottom of each sample was in contact with their corresponding anode.

Macroscopic morphological analysis has been performed using an X-ray tomograph (Somatom Sensation 64, Siemens, Munich, Germany). This tomograph has been used in previous studies on carbon anode characterization and all experimental and calculation details can be found in [13,14]. In summary, X-ray computed tomography (CT) allows 3D density analysis without damaging the sample structure. The output of the CT scanner is a 3D volume, reconstructed with images made of voxels. In the present study, the voxel size is $0.1453 \times 0.1453 \times 0.4 \text{ mm}^3$. The instrument response unit for each voxel is the Hounsfield Unit (HU), which is linearly related to the X-ray absorption coefficient. In the Hounsfield scale, air (STP conditions; STP: Standard temperature and pressure) has a value of -1000 HU and distilled water (STP conditions) has a value of 0. In term of grayscale image, the brighter the voxel, the denser the material. This information can then be used to evaluate the density ($\text{kg}\cdot\text{m}^{-3}$). Depending of the voxel resolution and sample microstructure scale, the density obtained may range from either the real to the macroscopically apparent. In the present case, most porosities are finer than the voxel dimensions therefore only the apparent density could be investigated and was expressed in Hounsfield scale (HU). The open source software ImageJ (version 1.51n, National Institutes of Health, Bethesda, MD, USA) was used for the CT data analysis.

For microstructure analysis, a scanning electron microscope (SEM; JEOL Ltd., Tokyo, Japan) has been used to obtain surface topology of the samples. The chemical analyses have been done with an NORAN energy dispersive spectrometer (Bruker, Billerica, MA, USA) coupled to the SEM.

3. Results and Discussion

3.1. Computed Tomography

3.1.1. Sample A

CT volume reconstruction of sample A is shown in Figure 2. The average X-ray absorption coefficient of the whole sample is around 1650 HU. Two orthogonal images along the sample length are shown in Figure 3 and are representative of the internal morphology of sample A. Their locations are represented by the yellow line and red line in Figure 2. Figure 3 clearly shows that sample A contains very large pores. These large pores (larger than the voxel resolution) comprise 3% of the sample volume in Figure 3a and 3.5% in Figure 3b. Hence, in that case, neglecting them may not have an important impact on the total frozen bath volume estimation through numerical investigation without considering the presence of gas. Furthermore, contrary to the observation made by Poncsák et al. [9] in laboratory experiments, no clear layer parallel to the anode surface is apparent in Figure 3. However, a “band layer” can be observed on Figure 3a. This structure may be relict of layers formed during freezing in conditions very different from the laboratory ones (e.g., heat flux non-perpendicular to the anode surface, local chemical composition variations, etc.). Spatial location of the frozen sample also seems to have an influence on density distribution, as highlighted on Figure 3b. Independent of the

large pores, frozen bath of Figure 3a exhibits a more homogeneous density distribution than the one in Figure 3b. Based on the laboratory observations of Poncsák et al. [9] in the transient case, it may be assumed that the frozen bath shown in Figure 3a has experienced a fast cooling rate leading to this more homogeneous density distribution. However, the density distribution shown in Figure 3b, leads to different conclusions. At this location (red line in Figure 2) the central part of the sample A is less dense than the outer region. This unconventional internal structure indicates freezing directionality in the central part that may be related to a change in the freezing direction related to an uncommon event in the cell. To highlight this, Figure 4 shows the X-ray absorption coefficient distribution and its histogram along the blue line, shown in Figure 3b. The histogram clearly reveals the two distinct zones. The middle part of the sample has an average of 1600 HU and this value increases to 1950 for the outer region, which corresponds to an increase of approximately 11% in term of density. Those values do not take into account the large porosities, observable at the far left of the histogram. As the denser region of the thicker part of the sample A is located around the sample, the density variations cannot be only related to the cooling rate, as observed by Poncsák et al. [9] in a controlled environment. Indeed, bath temperature of the cell may have changed due to changing flow conditions during the freezing: A parcel of bath with a higher or lower temperature may have passed the site of sample A, a possible consequence of turbulence in the bath or a wave on the bath metal interface. Such a change in the bath temperature could change the cooling rate (and chemistry), leading to a less orderly structure than would be seen in a lab sample.

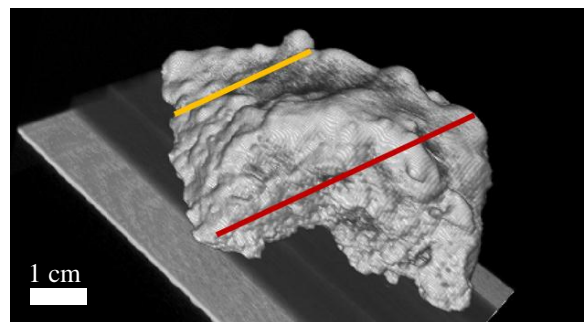


Figure 2. Volume reconstruction of sample A based on X-ray tomography.

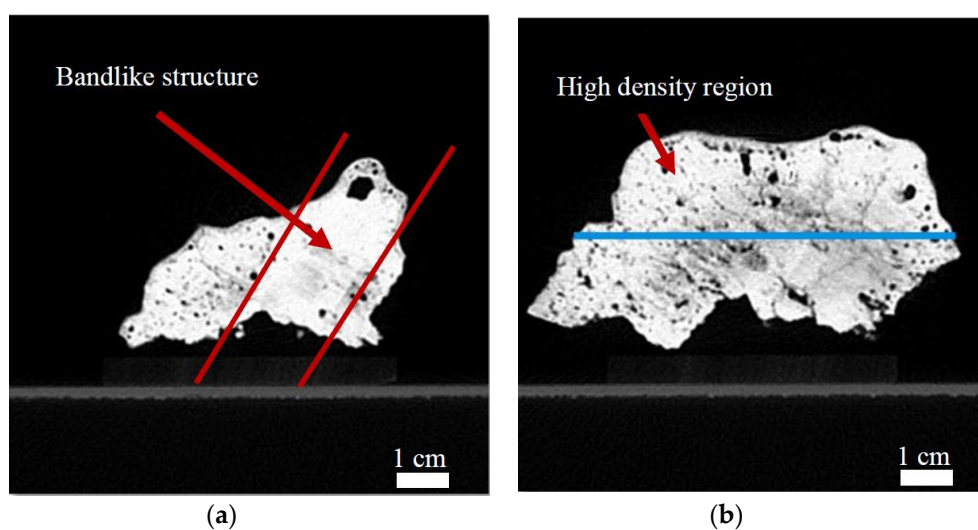


Figure 3. X-ray images of sample A: (a) Location represented by the yellow line in Figure 2 and bandlike structure (highlighted by the red lines); (b) location represented by the red line in Figure 2.

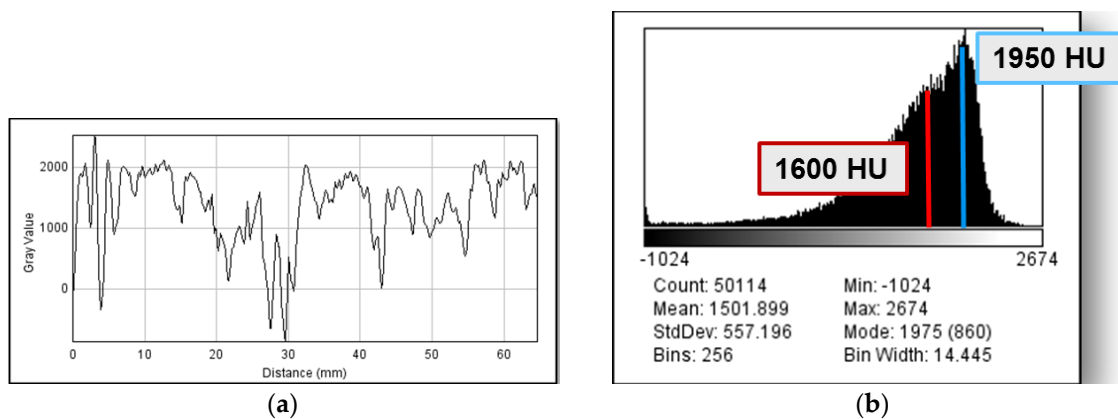


Figure 4. X-ray absorption coefficients (HU) distribution (a) and histogram (b) at the middle height of Figure 3b (blue line).

3.1.2. Sample B

CT volume reconstruction of sample B is shown in Figure 5. The average X-ray absorption coefficient of the whole sample is 1211 HU. Two orthogonal images along the sample length are shown in Figure 6 and are representative of the internal morphology of sample B. Their locations are represented by the yellow red lines in Figure 5, respectively. As expected from the external observation, internal structure of the sample B is very porous (Figure 6). It is also very clear that it contains very large pores. These large pores (larger than the voxel resolution) account for 10% in Figure 6a and close to 16% in Figure 6b. Hence, in that case, neglecting this porosity level will have an important impact on the estimation of total frozen bath volume in numerical simulation without considering gases. Morphology of sample B being very different from the sample A may reveal that cooling conditions (e.g., heat flux and fluid flow velocity) were very different in both cases. At this point, these are only assumptions that will have to be addressed in further investigations.

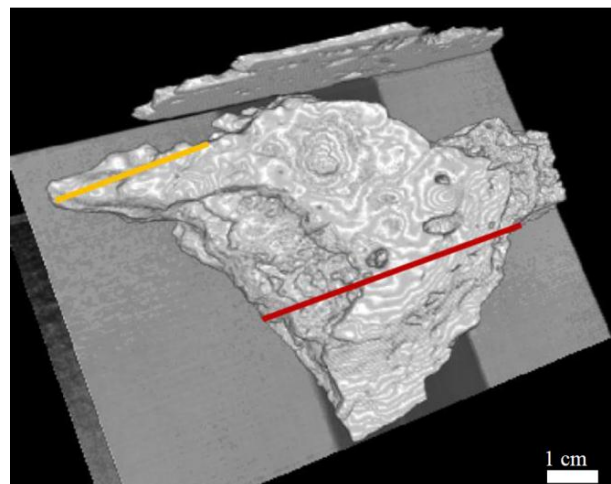


Figure 5. Volume reconstruction of sample B based on X-ray tomography.

Contrary to the observation made on sample A, sample B seems to have two distinct layers as shown in Figure 6. As observed experimentally by Poncsák et al. [9], the bottom layer, which has been very close to the cold anode surface, is more homogeneous than the outer layer. The latter is very brittle, very porous and contains most of the large pores. Spatial location of the frozen sample also seems to have an influence on density distribution, as highlighted on Figure 6, but to a lesser extent. If the large pores are neglected, the frozen bath in the outer layer (the more porous one) in

both Figure 6a,b tends to have a homogeneous density distribution. This is highlighted in Figure 7 by showing the X-ray absorption coefficient distribution and its histogram along the blue line shown in Figure 6b. The average X-ray absorption coefficient in this zone is approximately 1500 HU. This value is very close to the one obtained in the lower density region of Figure 3 (central part of sample A) indicating that both zones may have similar chemical composition. Again, this value does not take into account the large pores, observable at the far left of the histogram. Even though sample B seems to fit better the observation of Poncsák et al. [9], relating the morphology to the cooling rate, a chemical analysis is required to get some insight on the composition of each layer.

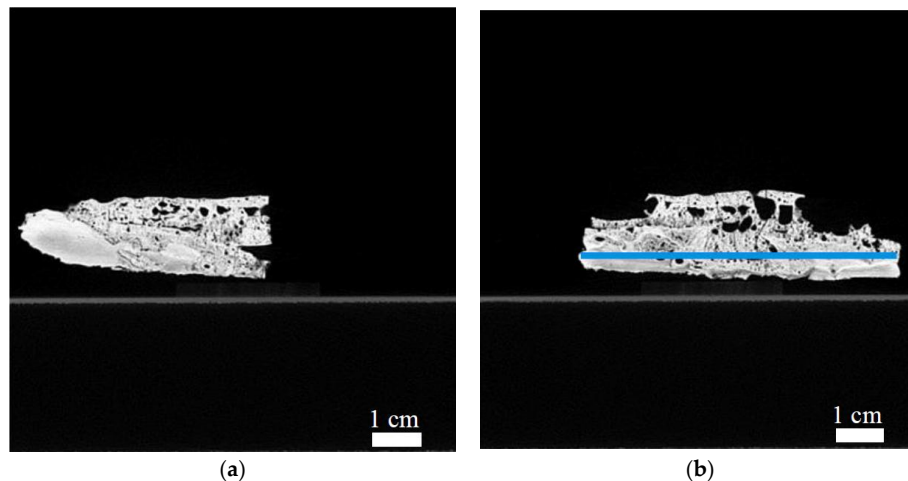


Figure 6. X-ray images of sample B: (a) Location represented by the yellow line in Figure 5; (b) location represented by the red line in Figure 5.

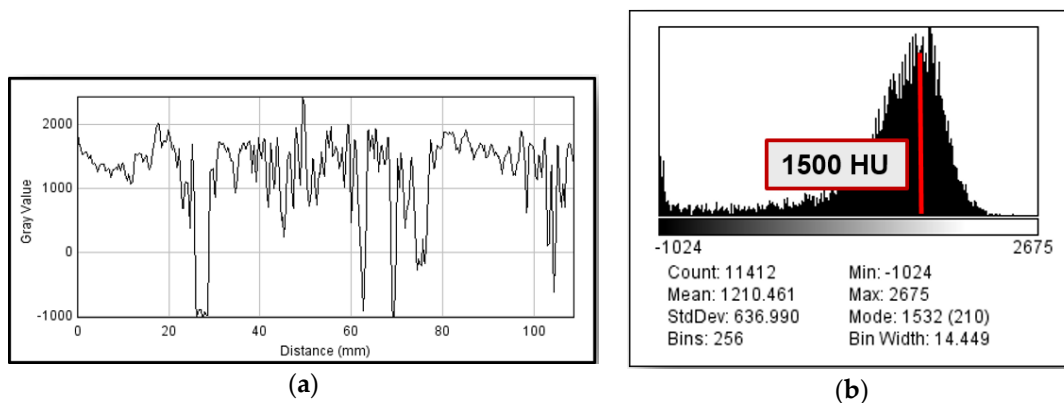


Figure 7. X-ray absorption coefficient (HU) distribution (a) and histogram (b) at the middle height of Figure 6b (blue line).

3.2. Scanning Electron Microscope/Energy-Dispersive X-ray Spectroscopy

Samples A and B both contain regions with different morphologies. The CT data was however not sufficient to identify the nature of these regions as they could not be directly related to cooling rate [9]. Chemical qualitative analyses were then performed on both samples using a SEM (15 kV) coupled with an EDS NORAN. The two regions of interest, denoted zone 1 and 2, were the macroscopically non-porous layers of sample B (bottom layer in Figure 6b) and the outer region of sample A (high density region in Figure 3b) respectively. Representative SEM images of the two regions of interest are shown in Figure 8. The high-density region (zone 2) seems to contain two types of structure: A large flaky zone and a small smooth and homogeneous one. On the other hand, zone 1 seems to contain

more of the smooth structure and less of the flaky one. EDS has then been used to identify those two distinguished zones and typical results are shown in Figure 9. The smooth structure (Figure 9a) contains mainly sodium (Na), fluorine (F) and aluminium (Al). Thus, this structure is most probably frozen cryolite (Na_3AlF_6). Oxygen (O) and calcium (Ca) were also detected. The oxygen may be related to alumina (Al_2O_3) while calcium is generally a good indicator of solid cryolite which can contain around 5% to 6% of CaF_2 . Gold (Au) and palladium (Pd) are related to the thin coating applied during surface preparation. On the other hand, the flaky zone mainly contains Al and O, which are probably related to alumina (Al_2O_3). This zone also seems to contain some cryolite (F and Na) as well as some calcium coming from the CaF_2 . Also, carbon (C) was found in both the smooth and the flaky structures. It may be assumed that this carbon is related to either anode dusting or to carbides. In the latter case, EDS could not be used to reveal the form of the carbide. As seen in Figure 1 (sample B), carbon dust seems to be indeed embedded within the sample, as observed in the dark zone. An SEM/EDS analysis of this region is shown in Figure 10. In that case, results show the presence of iron (Fe) and nickel (Ni), in addition to alumina and cryolite. These impurities come most probably from the anode [15]. Based on those analyses, the bottom layer of sample B (which was in contact with the anode) is mostly cryolite frozen at high cooling rate, as observed by [9] in laboratory. However, the presence of gas, alumina and carbon dust have affected the morphology of the upper layer of the sample B and the whole volume of sample A. Hence, the results differ, unsurprisingly, from the laboratory observations.

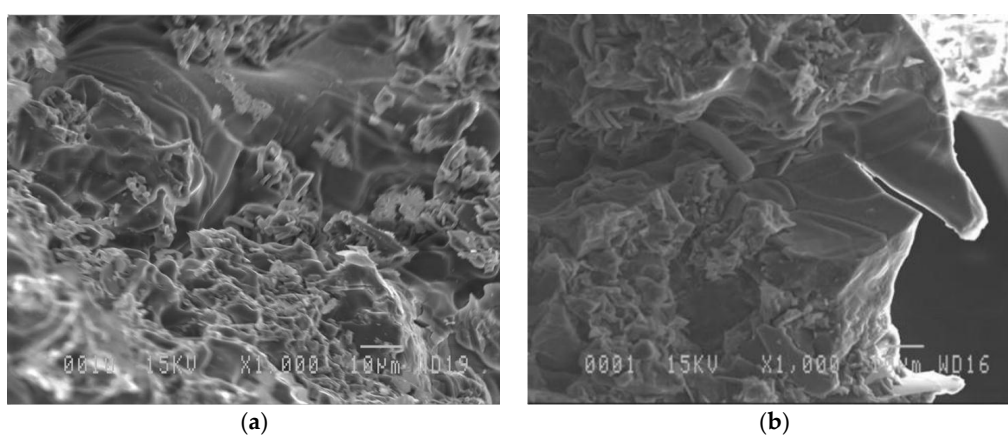


Figure 8. SEM (scanning electron microscope) representative images of investigated zone: (a) Zone 1; (b) zone 2.

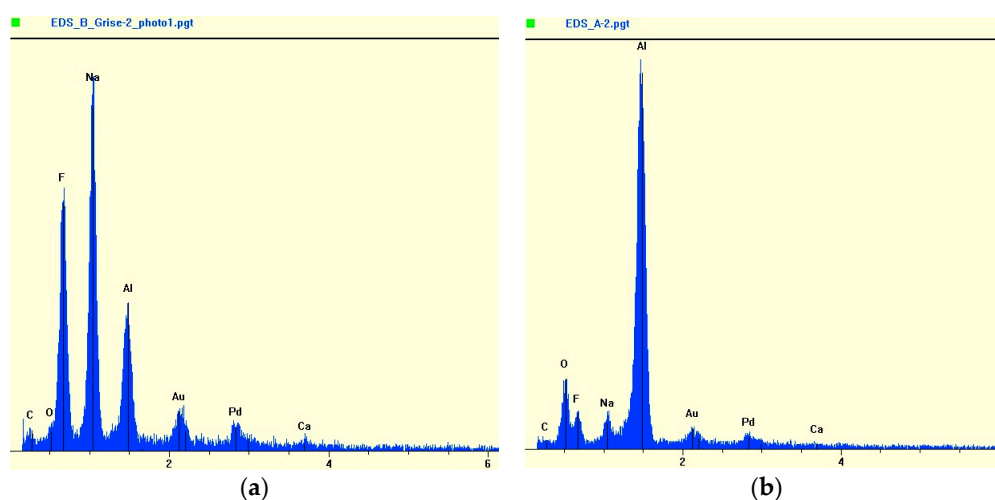


Figure 9. Typical results of EDS (energy-dispersive X-ray spectroscopy) analysis: (a) Smooth and homogeneous zones; (b) flaky zones.

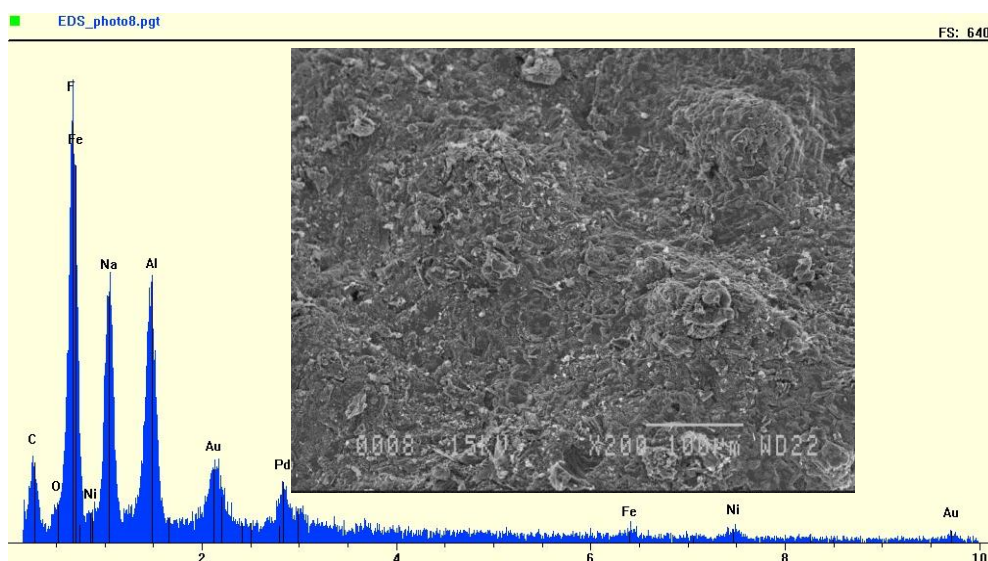


Figure 10. Typical results of SEM/EDS analysis of the dust containing region of Figure 1 (sample B).

4. Conclusions

Two bath samples that froze under newly-inserted anodes have been investigated with computed tomography and SEM/EDS methods to highlight the difference between the observations in industrial and laboratory conditions. The two samples were mainly chosen based on their very different morphologies. In both cases, the CT reveals a large variation in the amount of big pores in the samples considered. The origin of those large pores is still under investigation. It may be assumed that they are related to unidentified gas movement mechanisms (e.g., expelling of dissolved gas from the bath during the freezing process). Except for those large pores, morphology of sample B seems to fit the experimental observations of Poncsák et al. [9] regarding the effect of cooling rate on the frozen cryolitic bath morphology. However, the sample A morphology differs largely from the laboratory observations. Since the conditions in which each sample was exposed are not well known this has to be further investigated in order to better understand the source of those differences. Finally, computed tomography reveals the importance of taking into account the presence of gases, which may lead to the formation of large pores in the frozen bath samples. Most models addressing the bath phase change problem do not take into account the presence of these pores. Hence, the error on the volume estimated of the frozen ledge underneath the anodes may in turn affect the evaluation of the thermal conductivity of the product, changing its freeze/thaw dynamics.

Acknowledgments: Authors would like to acknowledge the financial support of the Natural Sciences and Engineering Research Council (NSERC) and Alcoa Corporation. A part of the research presented in this paper was financed by the Fonds de Recherche du Québec-Nature et Technologie (FRQNT) by the intermediary of the Aluminium Research Centre—REGAL.

Author Contributions: Donald Picard, Jayson Tessier, Guillaume Gauvin, Houshang Alamdari and Mario Fafard conceived and designed the experiments; Donald Picard, Jayson Tessier and Guillaume Gauvin performed the experiments; Donald Picard, Jayson Tessier, Guillaume Gauvin and Donald Ziegler analyzed the data; Jayson Tessier and Donald Ziegler contributed reagents/materials/analysis tools; Donald Picard, Jayson Tessier and Guillaume Gauvin wrote the paper.

Conflicts of Interest: The authors declare no conflict of interest.

References

1. Thonstad, J. Aluminum electrolysis electrolyte and electrochemistry. *Adv. Molten Salt Chem.* **1987**, *6*, 73–126.
2. Sørli, M.; Øye, H.A. *Cathode in Aluminium Electrolysis*, 3rd ed.; Aluminium-Verlag Marketing & Kommunikation GmbH: Düsseldorf, Germany, 2010.

3. Gusberti, V.; Severo, D.S.; Schneider, A.F.; Pinto, E.C.V.; Vilela, A.C. Modeling the Effect of the Anode Change Sequence with a non-Linear Shallow Water Stability Model. In *Light Metals 2007*; Sorlie, M., Ed.; Minerals, Metals & Materials Society: Warrendale, PA, USA, 2007; pp. 157–164.
4. Qiang, W.; Baokuan, L.; Fafard, M. Effect of anode change on heat transfer and magneto-hydrodynamic flow in aluminum reduction cell. *JOM* **2016**, *68*, 610–622.
5. Wang, Q.; Sun, M.; Li, B.; Peng, J.; Wang, Y. Numerical Investigation on the Impact of Anode Change on Heat Transfer and Fluid Flow in Aluminum Smelting Cells. In *Light Metals 2016*; Williams, E., Ed.; Minerals, Metals and Materials Society: Nashville, TN, USA, 2016; pp. 321–325.
6. Chartrand, P.; Pelton, A.D. A Predictive Thermodynamic Model for the Al-NaF-AlF₃-CaF₂-Al₂O₃ System. In *Light Metals 2002*; Schneider, W.A., Ed.; Minerals, Metals and Materials Society: Seattle, WA, USA, 2002; pp. 245–252.
7. Solheim, A.; Stoen, L.I.R. On the Composition of Solid Deposits Frozen Out from Cryolitic Melts. In *Light Metals 1997*; Huglen, R., Ed.; Minerals, Metals & Materials Soc (TMS): Orlando, FL, USA, 1997; pp. 325–332.
8. Li, M.; Chaouki, H.; Fafard, M.; Robert, J.L.; Ziegler, D. *Ledge Formation under the Consideration of Its Interaction with Bath Composition and the Fluid Dynamic Motion*; Université Laval: Québec, QC, Canada, 2015.
9. Poncsak, S.; Kiss, L.; Raymond, V.D.; Kaszas, C.; Guerard, S.; Bilodeau, J.F. Impact of the Heat Flux on Solidification of Cryolite Based Bath. In *Light Metals 2016*; Williams, E., Ed.; Minerals, Metals and Materials Society: Nashville, TN, USA, 2016; pp. 359–364.
10. Poncsak, S.; Kiss, L.I.; Guérard, S.; Bilodeau, J.F. Impact of the Solidification Rate on the Chemical Composition of Frozen Cryolite Bath. In Proceedings of the 34th International ICSOBA Conference, Quebec, QC, Canada, 3–6 October 2016.
11. Poncsak, S.; Kiss, L.; Belley, A.; Guerard, S.; Bilodeau, J.F. Study of the Structure and Thermophysical Properties of the Side Ledge in Hall-Héroult Cells Operating with Modified Bath Composition. In *Light Metals 2015*; Hyland, M., Ed.; Minerals, Metals and Materials Society: Orlando, FL, USA, 2015; pp. 655–659.
12. Poncsak, S.; Kiss, L.; St-Pierre, R.; Guerard, S.; Bilodeau, J.F. Structural Characterisation and Thermophysical Properties of the Side Ledge in Hall-Héroult Cells. In *Light Metals 2014*; Grandfield, J., Ed.; Minerals, Metals and Materials Society: San Diego, CA, USA, 2014; pp. 585–589.
13. Picard, D.; Alamdari, H.; Ziegler, D.; Dumas, B.; Fafard, M. Characterization of Prebaked Carbon Anode Samples Using X-Ray Computed Tomography and Porosity Estimation. In *Light Metals 2012*; Suarez, C.E., Ed.; Minerals, Metals and Materials Society: Orlando, FL, USA, 2012; pp. 1283–1288.
14. Picard, D.; Alamdari, H.; Ziegler, D.; St-Arnaud, P.O.; Fafard, M. Characterization of a Full-Scale Prebaked Carbon Anode Using X-Ray Computerized Tomography. In *Light Metals 2011*; Lindsay, S.J., Ed.; Minerals, Metals and Materials Society: San Diego, CA, USA, 2011; pp. 973–978.
15. Chevarin, F.; Lemieux, L.; Ziegler, D.; Fafard, M.; Alamdari, H. Air and CO₂ Reactivity of Carbon Anode and its Constituents: An Attempt to Understand Dusting Phenomenon. In *Light Metals 2015*; Hyland, M., Ed.; Minerals, Metals and Materials Society: Orlando, FL, USA, 2015; pp. 1147–1152.

